Journal of Multidisciplinary Engineering Science and Technology (JMEST)
ISSN: 2458-9403
Vol. 7 Issue 11, November - 2020

Characterization of Large-Scale Coherent Structures before and after Implanting Stent Graft into Specific Patient's Abdominal Aortic Aneurysm

Taewon Seo
Department of Mechanical and Automotive Engineering, Andong National University, Andong, Korea
dongjin@anu.ac.kr

Sun-Young Choi
Department of Radiology, Medical Center, Ewha WOMANS University, Seoul, Korea

***Abstract*— Aneurysm rupture occurs when the force balance between blood pressure and wall strength fails. It occurs mainly in area of flow recirculation where the wall shear stress (WSS) is significantly low and thrombus dominates. We extracted and generated the blood vessel models using MIMICS, a commercial software, through medical CT image files of patients before and after stent graft implantation provided by Medical Center of Ewha Womans University in Seoul, Korea. In order to investigate the effect of risk factors on rupture, we analyzed the effect of vortical structures with the aid of numerical techniques of CFD. In AAA models before stent graft implantation, vortices were heterogeneously distributed, whereas in the vascular models after EVAR, they were uniformly distributed. Vortices in AAA were generated and formed in the posterior region, and spread into the anterior zone. WSS acting on the normal blood vessel model is greater than WSS acting on the models of AAA, but WSS after EVAR is similar to the values acting on the normal blood vessel. This study provides useful information for deeper understanding of the characteristics of vortex structure of AAA.**

Keywords—Vortex structure; Stent-graft in AAA; CFD; Wall shear stress

I. INTRODUCTION

An aneurysm is defined as being at least 1.5 times bigger than the normal blood vessel size. Generally, an abdominal aortic aneurysm (AAA) is considered an aneurysm if the abdominal artery is greater than 30mm in diameter and the iliac artery is more than 18mm [1, 2]. Most AAA is fusiform and has large aortic bifurcations, but it also has saccular or other deflective structures, which are known to have a high risk of rupture [3-5].

There are three main causes of aortic aneurysm: atherosclerosis, non-infectious vasculitis, and vasculitis. Atherosclerosis is the most common cause of aortic aneurysm. Aortic aneurysm is a disease that develops with hypertension as well as with problems within the inner wall of arteries. The high pressure acting on the artery causes stress on the inner wall of the vessel, which reduces the elasticity of the vessel wall that causes the vessel wall to stretch. Non-infectious vasculitis is an inflammation of the blood vessel caused by autoimmune diseases or other causes, resulting in an elongation in the blood vessel wall. The last cause is arteritis caused by infection. When vasculitis in the aorta due to bacteria occurs, the tissues are loosened due to inflammatory reactions and the vessel wall is stretched to cause an aneurysm.

In general, an aneurysm is usually asymptomatic before rupture, and thin patients rarely feel the pulsating sensation in their stomach. A diagnosis is usually done by CT (Computerized Tomography), a non-invasive test [6].

Aortic aneurysm has a very low survival rate when ruptured so it needs to be treated. The standard criterion for treatment before an aneurysm rupture is based on the diameter of aortic aneurysm. When the diameter of an aortic aneurysm is more than 6cm, the diameter of the aneurysm is significantly increased and the risk of rupture is greatly increased [7, 8]. Also, if the aneurysm diameter increases by more than 5mm for 6 months, the risk of rupture increases significantly. Korea's insurance standard is that if AAA is more than 5cm or aneurysm growth over 5mm in 6 months, it is actively treated even before rupture. If a rupture seems likely, it is recommended that endovascular interventionist performs treatments (either surgery or stent graft) to help a patient survive, regardless of the size of the aneurysm. From a biomechanical point of view, a rupture occurs when the wall stress exerted on the aneurysm wall exceeds the yield strength on aorta [9].

There are four criteria for the treatment of AAA, which must all be treated. The first case is when the diameter of a AAA is greater than 5cm or the diameter of iliac artery is larger than 3cm. The second case is when the six month aneurysm expansion rate is greater than 0.5cm. The third is distal

thromboembolism in case of partial thrombosed abdominal aortic aneurysm, and the last is rupture.

If the maximal aortic neck diameter is greater than 32mm, the aortic neck length is greater than 15mm, and aortic neck angulation is less than 60°, then the endovascular aortic repair (EVAR) is suitable [10-12]. Thus endovascular stent graft, one of the treatments for AAA, can't be applied in all patients. In the case of stent grafting, the risk of endoleak [13-15] is high. In this case, a surgery is strongly recommended. However, since the mentioned criteria are not absolute standards, an endovascular interventionist can determine according to his or her experience and the characteristics of stent graft used.

A rupture in the blood vessel occurs when the equilibrium between the blood pressure and the wall mechanical strength is broken. Although it is not currently reliable to evaluate the risk of rupture based on the diameter of an aneurysm, its size is used as a criterion to predict the risk of rupture [16, 17]. It has been reported [18, 19] that aneurysm rupture occurs in the flow recirculation zone where the WSS is significantly lower and vascular thrombus is predominant. Numerous studies evaluating the risk of AAA report that the aneurysm geometry, such as a neck angle, neck length, and aneurysm size, is a significant factor in an aneurysm rupture [9, 11, 20].

The flow impingement regions formed by blood flow entering the aneurysm are known to have a particular pattern of WSS and pressure distribution [21-23]. The apex of flow impingement zone where flow stagnation occurs is characterized by low WSS and higher static pressure. It has been recently reported [24, 25] that the high WSS occurs at the area of proximal neck entering inside AAA. The formation, growth and rupture of AAA correlate with the areas of impingement and high WSS.

The aim of this study is to analyze the characteristics of large-scale vertical structures before and after stent graft implantation in two different specific patients' AAA geometries (see Fig. 1-b1, -b2, -c1 and c-2) in order to determine the risk factors for rupture. To achieve this, we applied computational fluid dynamics (CFD) to better understand the influence of large-scale coherent structures [26] before and after endovascular stent grafting of two different patients' AAA geometries compared to the flow characteristics of normal abdominal aorta (see Fig. 1a). Since the basic mechanism associated with the endothelial cell dysfunction of arterial wall that forms an atherosclerosis depend on the characteristics of hemodynamics, the numerical analysis will examine the relation between large-scale vertical structures and the effective index of WSS [27-30].

II. Materials and Methods

A. *Image Acquisition and Model Geometries*

CT scan image data in the study were acquired by SOMATOM Sensation 64 (Siemens Medical Solutions, Germany) from healthy patients at the Medical Center of Ewha Womans University in Seoul, Korea. The geometric information about the blood vessel models of patients extracted using Mimics 16.0 (Materialise, Belgium) is presented in Table 1. The suitable realistic abdominal aortic geometrical models in Fig. 1 (1a, 1-b1, 1-b2, 1-c1, 1-c2) were generated from these DICOM files using Mimics software. Fig. 1-b2 and –c2 are the patient's vascular models after 6 months since the stent graft implantation. After loading the image files into MIMICS, the user can see images in the axial (XY plane), coronal (XZ) and sagittal (YZ) directions. The most important first step to convert the image files to a 3D model is a segmentation process. During segmentation the user creates 3D model based on the gray values within these DICOM files using thresholding. The user can apply the "region growing" tool to remove any floating pixels in the images and to separate the bone from the blood vessel. Finally the geometry model is obtained using the image segmentation and 3D model generated by the commercial software package workbench, ANSYS v19.0 (ANSYS Inc., Canonsburg, PA).

B. *Governing Equations and Numerical Methods*

The computations involve solving the governing equations as Navier-Stokes equations for incompressible, homogenous, laminar and Newtonian flow. Blood is modeled as Newtonian fluid with blood density (ρ=1,050 N/m^3) and blood dynamic viscosity (μ=0.0035 Pa·s).

Rigid abdominal aortic walls assumption is used to simplify the computation. Thus, the mass and momentum conservation equations for an incompressible Newtonian fluid neglecting the influence of body force, such as gravity, can be written as:

Continuity:

$$\frac{\partial u_i}{\partial x_i} = 0 \qquad (1)$$

Linear momentum:

$$\rho\left[\frac{\partial u_i}{\partial t} + \frac{\partial (u_i u_j)}{\partial x_j}\right] = -\frac{\partial p}{\partial x_i} + \mu \frac{\partial}{\partial x_j}\left(\frac{\partial u_i}{\partial x_j}\right) \qquad (2)$$

where u_i denote the blood velocity in the i direction (i, j runs from 1 to 3, respectively).

For inlet boundary, a time-dependent physiological velocity profile at the inlet is shown in Fig.2a. The inlet velocity applied is the physiological velocity waveform Molongy *et al* [31]. The Reynolds numbers at the maximal, minimal and mean rates of blood flow at the proximal inlet were approximately 1,890, 25 and 670, respectively [29, 32]. The peak systolic flow occurred at t=0.25 s as shown in Fig. 2a. The Womersley number, α, is defined by $\alpha = \frac{d}{2}\sqrt{\frac{\rho\omega}{\mu}}$. ω represents the angular frequency of the pulsatile flow and d is the normal diameter of inlet. In this simulation, the

Womersley number at the proximal inlet was approximately 13.73.

In Fig. 2a, six different times (t_1, t_2, t_3, t_4, t_5, t_6) were selected to analyze the hemodynamic behaviors. The inflow at the inlet of abdominal artery accelerates early in the inlet velocity temporal waveform, t_2=0.15s, and reaches the maximum of 0.31 m/s at t_3=0.25 s. After this point, the velocity magnitude begins to decrease at t_4=0.35 s and drops to a retrograde flow during the diastolic phase at t_5=0.50 s [32]. Then, the blood flow slightly oscillates to reach the second peak velocity at t_6=0.80 s and decreases to the second minimum velocity at t_1=0.10 s. The pressure boundary condition is applied at the outlet in this study as shown in Fig. 2b. A no-slip condition was applied on the arterial walls.

The governing equations were solved using the commercial software package FLUENT, ANSYS 19.0 (ANSYS Inc., Canonsburg, PA). The quick scheme was used to discretize the momentum and the second order scheme applied pressure variables using the PISO (Pressure Implicit with Splitting of Operators) algorithm. The implicit time-marching first-order scheme with the time step t=0.01 was used for the calculations, and the maximum iterations per time step was set to 2,000.

To establish mesh independence of our numerical results, we tested mesh independence in the 0.8 to 2.8 million polyhedral mesh ranges. In order to get the numerical solutions that do not depend on the mesh, we applied 1.6 million meshes. The governing equations were discretized with finite volume method (FVM) using commercial software, FLUENT in ANSYS v19. The PISO algorithm is applied to solve pressure-velocity coupling. To obtain the stable solutions, the computation performed four cardiac cycles and the result at the fourth cardiac cycle was used for the analysis in order to decrease the numerical errors compared to the result at the third cardiac cycle less than 1%. The convergence tolerance for the continuity and velocity residuals was set at 10^{-5}. The PCs used for simulations were based on the Intel® Xeon ® CPU E5-2667 two processors with 2.9GHz clock speed and 64GB RAM memory running on the 64 bit Windows 7. The simulation time for the computational domains used in the study was approximately 31 CPU hours on average.

III. RESULTS

It is hard to obtain the comparable actual baseline data to verify the results obtained in this study. Thus, we extracted a normal AA model from CT images, conducted the simulation and used the numerical results as the baseline data. To verify the formation and propagation of large vortices, we compared large vortex structures in models A and B extracted before and after stent graft implantation from CT medical imaging data of patients A and B with baseline data for healthy AA model C (see Fig. 1a). The geometrical model from AAA of patient A had the neck angulation geometry of 30^o while that of patient B was measured to be 84^o.

A. The Comparison of Hemodynamic Characteristics among the Model Geometries

Fig. 3 illustrates the results of streamlines in AAA models before and after stent graft implantation at peak systole, mid-deceleration and early diastole of patients A and B. When the blood flow enters AAA at peak systole, the blood flow with strong momentum tends to flow without recirculation in the anterior by the force straight downward as shown in Fig. 3a (see patient A and B Pre). At the peak systole the blood flow entering the proximal neck of AAA has an impingement on the anterior wall of AAA. On the other hand, a large cavity is created in posterior in AAA and a weak recirculation is formed due to the entrainment of a small amount of blood flow as shown in Fig. 3a (see Fig. 3a patient A and B Pre). During the cardiac cycle, the velocity of blood flow decelerates (at point 4 in Fig. 2a) and, passes through the diastolic phase (at point 5 in Fig. 2a), and the blood flow in AAA spreads throughout the aneurysm with large recirculation towards the posterior wall in AAA (see Fig. 3b and c of patient A and B Pre). The flow patterns in AAA proximal neck region before the procedure are complex, during deceleration and diastolic phases. In contrast, the flow after the procedure becomes stable as it passes the acceleration phase during cardiac cycle.

As shown in Table 1, the neck angle of patient A is 30^o and that of patient B is 84^o. When comparing the flow characteristics in AAA of patients A and B, the swirling of instantaneous velocity streamlines is formed in the proximal of posterior side for patient B as it proceeds toward the distal sac of aneurysm and appears coiled up.

Although the results for blood flow through a normal abdominal aortic model are not shown, we can see that the blood flow in AAA model were stent grafts are inserted has the same flow pattern as in a normal AA model. Put another way, we can see that the flow pattern in which stent graft is implanted flows smoothly without recirculation at peak systole (see patient A and B Post in Fig. 3). Additionally, the pattern of blood flow during the deceleration and diastolic phases after stent graft implantation is different from the pattern of blood flow before the procedure.

Fig. 4 shows the iso-surface of vorticity magnitudes at peak systolic, mid-deceleration, and at diastolic phases of patients A and B. A vortex occurs in the flow region near the wall with shear. Therefore, we can see that the vortices are formed on the anterior side with large shear and the posterior side with small shear in Fig 4 for patients A and B pre. The vortices in the aneurysm before the stent procedure are heterogeneously distributed (see patient A and B Pre in Fig. 4), but after the stent implantation, they are

homogeneously distributed throughout the model (see patient A and B Post in Fig. 4).

Fig. 5 represents the vorticity in the x-direction in the mid sagittal (yz-plane) and the vorticity in the z-direction in the mid coronal cross-sections (xz-plane) of AAA of patients A and B. In the case of patient A in the sagittal cross-section, the jet-like structure enters the aneurysm at the peak systole and breaks into a smaller vortex structure at the decelerating phase during the cardiac cycle. In the diastolic phase, the small vortices in AAA show a very complex flow pattern and are evenly distributed. In patient B, the vortex distribution in the sagittal plane in AAA is similar to that of patient A. In both patients A and B, the jet-like structure penetrated into the AAA through the neck spreads widely downward as it progresses to the anterior wall. Both the forward and backward vortical structures indicate in the entire aneurysm during the cardiac cycle. In the coronal plane of both patients A and B the streamwise vortices are largely formed toward the lateral wall and can be seen flowing downward.

Fig. 6 shows the streamwise vorticity in the transverse mid plane before and after stent implantation of patients A and B at peak systolic, mid-deceleration, and at diastolic phases during the cardiac cycle. At peak systole, the strong vortex in the clockwise direction for AAA model of patient A proceeds in the downstream direction near the anterior wall, and the weak vortex in the counterclockwise direction occurs in the posterior side wall in the cavity region. Along the cardiac cycle, the vortex near the posterior wall grows and spreads to the anterior wall (see Fig. 6b ad c, patient A pre). As shown in patient A pre, the blood flow in the vicinity of anterior region flows downward with rotating clockwise, while it flows upward with rotating counterclockwise in posterior region. As seen in patient B pre, the streamwise vorticity formed during peak systole on the posterior side grew and penetrated over time in the direction of abdominal cavity. Later in the cardiac cycle, we observe a higher level in streamwise vorticity for both in patients A and B pre once chaotic flow patterns have increased significantly (see Fig. 3). In this case the initial roll-up of vortical structure breaks down in smaller ones once the flow decelerates due to the adverse pressure gradient.

B. Comparison of WSS among the Model Geometries

The WSS distributions in a normal artery and that of AAA models of patients A and B at peak systolic, at mid-deceleration and at diastolic phases during the cardiac cycle are depicted in Fig. 8. At peak systole, the high WSS regions are located at the proximal below the neck angulation and over the aneurysm sac for both patients A and B pre as seen in Fig. 7a. In the decelerating and diastolic phases during the cardiac cycle, the peak WSS acting on the aneurysm moves from proximal to distal regions on the anterior side of AAA. A large WSS is produced as a result of the impact of vortex on the anterior wall (see Fig. 4). The WSS distributed in the aneurysm of patients A and B is lower than WSS acting on the normal AA. On the other hand, after the stent graft implantation the WSS on the blood vessel is distributed similarly to the value acting on the normal AA.

Fig. 8 depicts the average magnitude of WSS along the surface of AAA for patients A and B normalized by surface area of healthy AA. WSS in healthy blood vessel ranges from 4.32 pa at the peak systolic to 0.17 pa at diastolic phases. In the case of patient A, the average magnitudes of WSS before stent graft implantation had an average value of about 73% or greater than that of healthy AA, whereas the average WSS after the procedure had a 79% increase compared to before the procedure. In patient B, WSS acting on the surface of AAA before and after stent graft implantation was lower than WSS in normal AA at 30% and 16.4%, respectively."

IV. DISCUSSION

Our study shows the computational numerical analysis of the characteristics of large-scale vertical structures in normal AA and patient specific AAA models before and after stent graft implantation. In this study, we analyzed two representations of AAA vessel geometries before and after stent graft implantation with different characteristics compared to a normal artery model. We generated the geometrical vascular models in the study from medical CT images, and performed analysis using ANSYS FLUENT v19.0 (ANSYS Inc., USA).

The primary criterion for determining the repair of AAA to prevent rupture is the aneurysm size [3-5, 11, 38]. In the models used in the study, the maximum aneurysm diameter of patient A was 42.15 mm and that of patient B was 55.58 mm as shown in Table 1. According to previously published papers [16, 17, 38], the risk of rupture is from 1% to 7% for aneurysm that is 4 cm to 5 cm in diameter, while the risk increases to 20% to 40% for aneurysm greater than 5 cm in diameter.

In the case of fusiform AAA models, which were computed in this study, systolic blood flows down to the proximal end of aneurysm, resulting in shedding of vortex structure during the early diastole. The vortex structure formed in AAA likely plays an important role in thrombus formation and inflammatory mechanisms, as well as activated platelets in the reattachment region where low WSS could adhere to the thrombogenic surface. In this study, the vortex structures generated near the proximal neck of AAA in the decelerating phase of the flow rate detaches and proceeds toward downstream, clearly showing that it impinges, and breaks up into two vortices on the anterior wall in the distal AAA wall (see Figs. 3, and 4). Several previous studies [10, 20, 26] have reported that during systolic phase the vortex formation occurs at the proximal neck of artery. During the systole in

the cardiac cycle, a high velocity blood flow enters the aneurysm in a suddenly enlarged cross-sectional area, creating an adverse pressure gradient, and thereby causing vortex formation and roll-up.

When comparing the size and length of aneurysms in patients A and B, the larger and longer the maximum diameter of AAA, the less the strength of large vorticity and smaller the flow disturbance in AAA as shown in Figs. 4~6. The large-scale vorticity structure is formed by separation at the proximal neck along the posterior wall of AAA, while the blood flow is accelerated in the cardiac cycle. This result shows a higher shear in this site compared to the anterior wall. We found that irregular vortices are formed in AAA. Additionally, the vortices formed this way flowed in the distal region to form a large vortex and greatly changed the shape of bloodstream. The vortex structure generated in the proximal neck during the decelerating phase propagates downstream during the cardiac cycle, impinging on the anterior wall in the distal AAA region. The study showed that the vortex structure breaks up and gets separated along the anterior wall in a counterclockwise circulation.

When the Stokes number was less than 1, the viscosity of the particles was very small and the particles tended to be concentrated in the core region of the vortex structures. Because of the vortices generated in AAA, platelets are trapped in the core region of the vortex structure, which progresses to the development of intraluminal thrombus [34, 36]. In this study, the order of magnitude of the Stokes number during the cardiac cycle is approximately 10^{-06}, that platelets in AAA will closely follow the flow pattern. Particles traveling along the vortex structure may undergo high shear, which can cause platelet activation. If platelets are activated, the platelets entering recirculation zone are likely to adhere to AAA wall and develop into thrombus deposition. Thrombus formed on the AAA wall will accelerate its degeneration.

The decision of stent graft implantation depends on the diameter of AAA, but if the diameter is greater than 5.5cm, then EVAR is recommended. However, a small diameter of AAA can sometime rupture. In this case, Stent graft implantation is required before a rupture occurs. In this study, patient A was treated with stent graft implantation when the aneurysm was small, while patient B was treated with a large diameter.

The neck area and the region where the blood flow jet is affecting aneurysmal sac had large WSS values. The lower WSS region also coincides with the location of recirculation region with low blood flow velocity (see Figs 5 and 8). In peak systole, the average WSS of patient B was lower than that of a normal aorta model. However, the average WSS of patient A was larger than that of a normal aorta model.

While the models applied in this study were geometries extracted from specific patients with AAA, the mechanical properties and boundary conditions used by Molongy *et al* [31] were applied in this study. Although this study has limitations in which we do not consider the elasticity of vessel wall and thrombus, the fluid-structure interaction may alter the characteristics in AAA. Further, the intra-luminal thrombus (ILT) can be found in most AAA, it has not been clarified whether it acts as buffer against WSS affecting AAA rupture or weakens vascular wall [39]. In addition, although Non-Newtonian effect is important in a complex domain with a small shear rate in large blood vessels [34], we assumed a Newtonian fluid model in the study. Biasetti *et al* [34] published that the predictions of WSS in Newtonian and Carreau-Yasuda models were almost the same.

Acknowledgement

This work was financially supported by Andong National University.

REFERENCES

[1] Johnston KW, Rutherford RB, Tilson MD, Shah DM, Hollier L, Stanley JC (1991) Suggested standards for reporting on arterial aneurysms. J Vasc Surg 13:452-458

[2] Maier A, Gee MW, Reeps C, Pongratz J, Eckstein HH, Wall WA (2010) A comparison of diameter, wall stress, and rupture potential index for abdominal aortic aneurysm rupture risk prediction. Ann. Biomed. Eng. 38(10): 3124-3134

[3] Vorp DA, Raghavan ML, Webster MW (1998) Mechanical wall stress in abdominal aortic aneurysm. Influence of diameter and asymmetry. J Vasc Surg 27:632-639

[4] Lederle FA, Wilson SE, Johnson GR, Reinke DB, Littooy FN, Acher CW, Ballard DJ, Gordon LM, Chute EP, Krupski WC, Bandyk D, Vet ADM (2002) Immediate repair compared with surveillance of small abdominal aortic aneurysms. N. Engl. K. Med. 346(19): 1437-1444

[5] Fillinger MF, Raghavan ML, Marra SP, Cronenwett JL, Kennedy FE (2002) In vivo analysis of mechanical wall stress and abdominal aortic aneurysm rupture risk. J Vasc Surg 36:589-597

[6] Moxon JV, Parr A, Emeto TI, Walker P, Norman PE, Golledge J (2010) Diagnosis and monitoring of abdominal aortic aneurysm: Current status and future prospects. Curr Probl Cardiol 35(10):512-548

[7] Hirsch AT, Haskal ZJ, *et al* (2005) Practice guidelines for the management of patients with peripheral arterial disease (Lower extremity, renal, mesenteric and abdominal aortic) Circul 113:e463-e654

[8] Roger VL, Go AS, Lloyd-Jones DM, et al (2012) Heart disease and stroke statistics. Circul 125:e2-e220

[9] Georgakarakos E, Ioannou CV, Papaharilaou Y, Kostas T, Katsamouris AN (2011) Computational evaluation of aortic aneurysm rupture risk: What have we learned so far? J Endovasc Ther 18:214-225.

[10] Algabri YA, Rookkapan S, Chatpun S (2017) Three-dimensional finite volume modeling of blood flow in simulated angular neck abdominal aortic aneurysms. IOP Cong. Seires: Materials Science and Eng 243

[11] Xenos M, Alemu Y, Zamfir D, Einav S, Ricotta JJ, Labropoulos N, Tassiopoulos A, Bluestein D (2010) The effect of angulation in abdominal aortic aneurysms: fluid-structure interaction simulations of idealized geometries. Med Biol Eng Comput 48:1175-1190

[12] Drewe CJ, Parker LP, Kelsey LJ, Norman PE, Powell JT, Doyle BJ (2017) Haemodynamics and stresses in abdominal aortic aneurysms: A fluid-structure interaction study into the effect of proximal neck and iliac bifurcation angle. J Biomech 60:150-156

[13] Lu YH, Mani K, Panigrahi B, Hsu WT, Chen CY (2016) Endoleak assessment using computational fluid dynamics and image processing methods in stented abdominal aortic aneurysm models. Comput Math Methods Medv2016:9567294

[14] Lu YH, Chen CY, Menon PG, Liu KT, Lin HH (2013) Hemodynamic effects of endoleak formation in abdominal aortic aneurysm patients with stent-graft implants. J of Med and Biolog Eng 34(6):554-558

[15] Schuurmann RCL (2017) A novel methodology for improved imaging analysis pre- and post-evar. Academic thesis, University of Twente

[16] Maier A, Gee MW, Reeps C, Pongratz J, Eckstein HH, Wall WA (2010) A comparison of diameter, wall stress, and rupture potential index for abdominal aortic aneurysm rupture risk prediction. Ann Biomed Eng. 38(10):3124-3134

[17] Volokh KY (2010) Comparison of biomechanical failure criteria for abdominal aortic aneurysm. J Biomech 40(10):2032-2040

[18] Cebral J, Mut F, Weir J, Putman C (2011) Association of hemodynamic characteristics and cerebral aneurysm rupture. Am J Neurorad 32:264-270

[19] Altuwaijri O (2012) Advanced computer modeling of abdominal aortic aneurysm to predict risk of rupture. Thesis, University of Hull

[20] Li Z, Kleinstreuer C (2006) Effects of blood flow and vessel geometry on wall stress and rupture risk of abdominal aortic aneurysms. J Med Eng Tech 30:283-297

[21] Boussel L, Rayz V, McCulloch C, Martin A, Acevedo-Bolton G, Lawton M, Higashida R, Smith WS, Young WL Saloner D (2008) Aneurysm growth occurs at a region of low wall shear stress: patient-specific correlation of hemodynamics and growth in a longitudinal study. Stroke 39(11):2997-3002

[22] Jou LD, Lee D, Morsi H, Mawad M (2008) Wall shear stress on ruptured and unruptured intracranial aneurysms at the internal carotid artery. Am J Neuroradiol 29:1761-1767

[23] Sforza DM, Putman CM, Cebral JR (2009) Hemodynamics of cerebral aneurysms. Annu Rev Fluid Mech 41:91-107

[24] Algabri YA, Rookkapan S, Gramigna V, Espino DM, Chatpun S (2019) Computational study on hemodynamic changes in patient-specific proximal neck angulation of abdominal aortic aneurysm with time-varying velocity. Australas Phys Eng Sci Med 42(1):181-190

[25] Seo TW, Choi SY (2019) Hemodynamic analysis for the impact of rupture risk factors of abdominal aortic aneurysmal geometric models. Trans Korean Soc Mech Eng B 43(4):261-269

[26] ArzaniA (2016) Hemodynamics and transport in patient-specific abdominal aortic aneurysms. Thesis, University of California,Berkeley

[27] Joly F, Soulez G, Garcia D, Lessard S, Kauffmann C (2018) Flow stagnation volume and abdominal aortic aneurysms growth: Insights from patient-specific computational flow dynamics of Lagrangian-coherent structures. Comp. Bio. And Med 92:98-109.

[28] Fytanidis DK, Soulis JV, Giannoglou GD (2014) Patient-specific arterial system flow oscillation Hippokratia 18(2):162-165.

[29] Poelma C, Watton PN, Ventikos Y (2015) Transitional flow in aneurysms and the computation of haemodynamic parameters. J. R. Soc. Interface 12:20141394.

[30] Baek H, Jayaraman MV, Richardson PD, Karniadakis (2010) Flow instability and wall shear stress variation in intracranial aneurysm. J. R. Soc. Interface 7:967-988.

[31] Molony DS, Callanan A, Kavanagh EG, Walsh MT, McGloughlin TM (2009) Fluid-structure interaction of patient-specific abdominal aortic aneurysm treated with an endovascular stent-graft. BioMedical Eng. Online 8:24

[32] Moghadam EM, Bazilevs Y, Hsia TY, Vignon-Clementel IE, Marsden AL (2011) A comparison of outlet boundary treatments for prevention of backflow divergence with relevance to blood flow simulations. Comput.Mech. 48:277-291.

[33] Trip R, Kuik DJ, Westerweel J, Poelma C (2012) An experimental study of transitional pulsatile pipe flow.Phys. Fluids 24, 014103 (doi:10.1063/1.3673611)

[34] Biasetti J, Hussain F, Gasser TC (2011) Blood flow and coherent vortices in the normal and

aneurysmatic aortas: a fluid dynamical approach to intra-luminal thrombus formation. J.R. Soc. Interface 8: 1449-1461.

[35] Deplano V, Meyer C, Guivier-Curien C, Bertrand E (2013) New insights into the understanding of flow flow dynamics in an in vitro model for abdominal aortic aneurysms. Med.Eng. & Phy. 35:800-809.

[36] Bluestein D, Gutierrez C, Londono M, Schoephoerster RT (1999) Vortex shedding in steady flow through a model of an arterial stenosis and its relevance to mural platelet deposition. Ann Biomed Eng. 27(6):763-773.

[37] Boyd AJ, Kuhn DCS, Lozowy RJ. Kulbisky GP (2016) Low wall shear stress predominates at sites of abdominal aortic aneurysm rupture. J Vasc Surg 63:1613-1619.

[38] Aggarwal S, Qamar A, Sharma V, Sharma A (2011) Abdominal aortic aneurysm: A comprehensive review. Exp Clin Cardiol 16(1):11-15.

[39] Qiu Y, Wang Y, Fan Y, Peng L, Liu R, Zhao J, Yuan D, Zheng T (2019) Role of intraluminal thrombus in abdominal aortic aneurysm ruptures: A hemodynamic point of view. Med Phys. 46(9):4263-4275.

[40] Di Martino ES Vorp DA (2003) Effect of variation in intraluminal thrombus constitutive properties on abdominal aortic aneurysm wall stress. Ann. Biomed. Eng. 31(7):804-809.

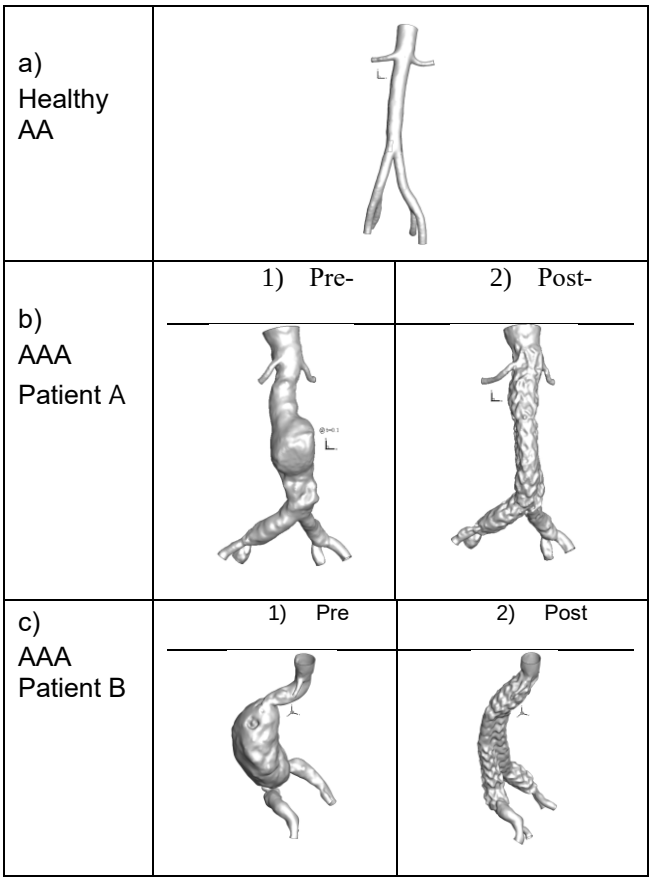

Fig. 1 3D geometries (a) for normal abdominal aorta, (b) for AAA patient A (c) for AAA patient B in before and after stent graft implantation

Table 1 Patient's geometric model information

Patient's Information	Patient A	Patient B	Healthy Patient C
Gender	F	M	M
Age	78	51	42
Inlet Diameter	28.51	19.54	19.33
Aneurysm Length (mm)	48.86	102.6	-
Proximal Neck Angle (Degree)	30°	84°	-
Aneurysm Diameter (mm)	42.15	55.58	-
Distal Left Iliac Diameter	9.3, 7.88	6.96, 4.67	6.68, 8.93
Distal Right Iliac Diameter	8.04, 8.25	8.2, 4.36	6.84. 9.05

a) Inlet velocity profile

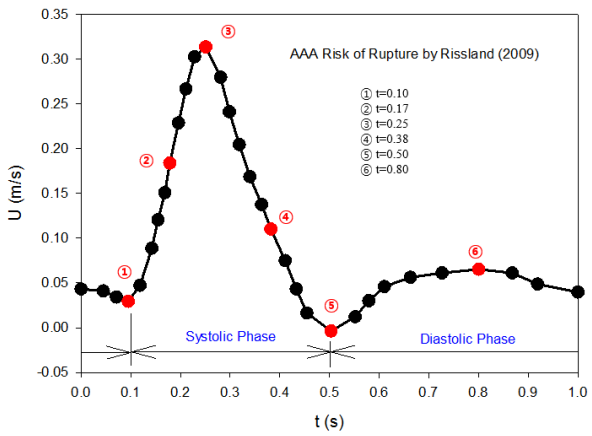

b) Outlet pressure distribution

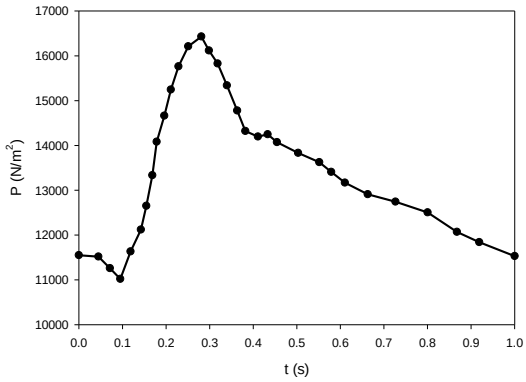

Fig. 2 Inlet velocity and outlet pressure waveforms

	a) t=0.25 (Peak Systole)
Patient A Pre	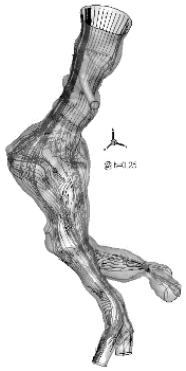
Patient A Post	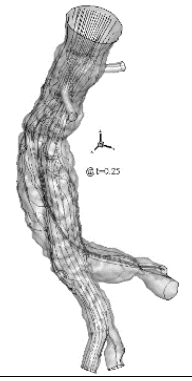
Patient B Pre	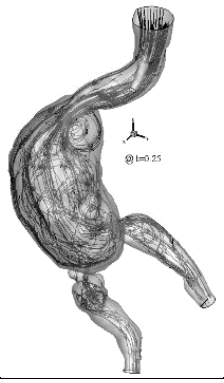
Patient B Post	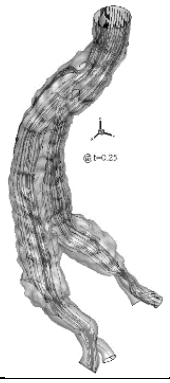
	b) t=0.38 (Mid Deceleration)
Patient A Pre	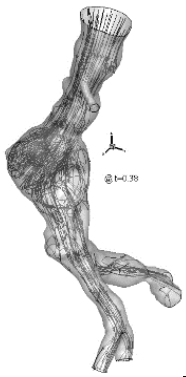
Patient A Post	
Patient B Pre	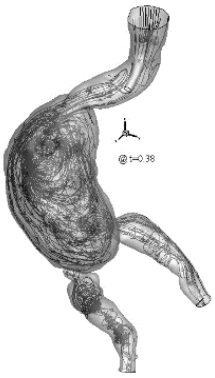

Patient B Post	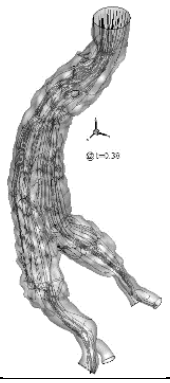
	c) t=0.5 (Early Diastole)
Patient A Pre	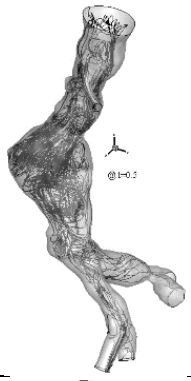
Patient A Post	
Patient B Pre	

Patient B Post	

Fig. 3 Comparison of streamline distributions of patients A and B at peak systolic, decelerating and diastolic phases during the cardiac cycle

	a) t=0.25 (Peak Systole)
Patient A Pre	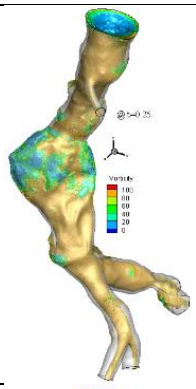
Patient A Post	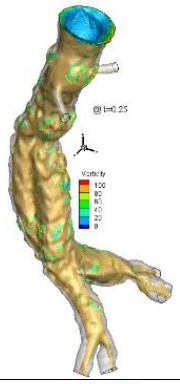
Patient B Pre	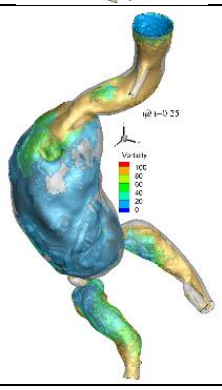

Patient B Post	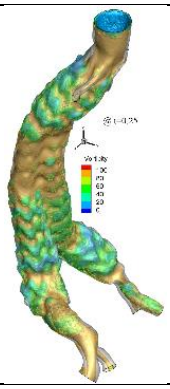	Patient B Post	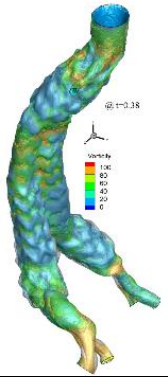
	b) t=0.38 (Mid Deceleration)		c) t=0.5 (Early Diastole
Patient A Pre	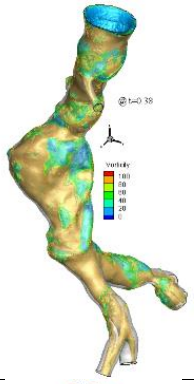	Patient A Pre	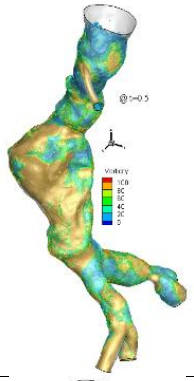
Patient A Post	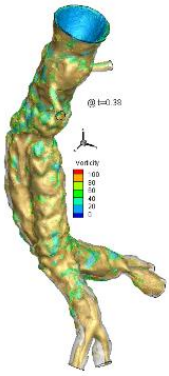	Patient A Post	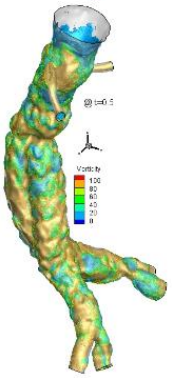
Patient B Pre	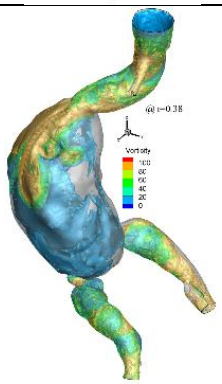	Patient B Pre	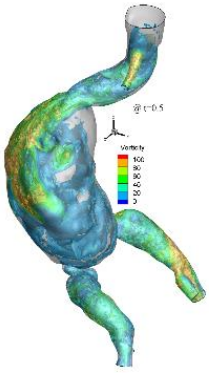

Fig. 4 Comparison of iso-surface magnitude of vorticity before and after the procedure in AAA of patients A and B at peak systolic, decelerating and diastolic phases during the cardiac cycle

Patient B Post	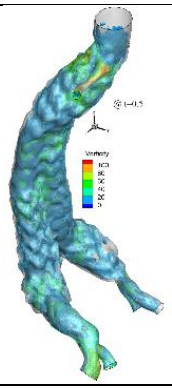

a) t=0.25 (Peak Systole)

Patient A Sagittal Plane	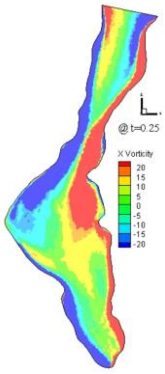
Patient A Coronal Plane	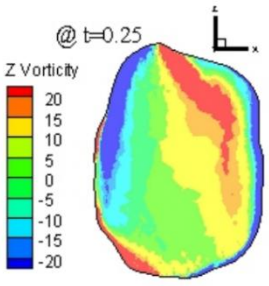
Patient B Sagittal Plane	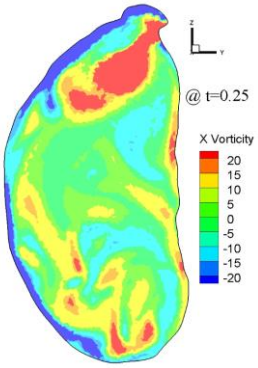

Patient B Coronal Plane	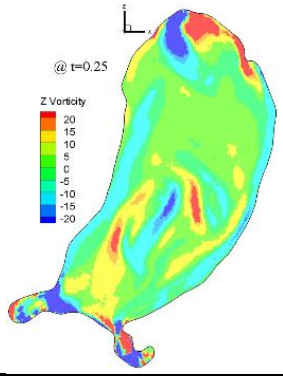

b) t=0.38 (Mid Deceleration)

Patient A Sagittal Plane	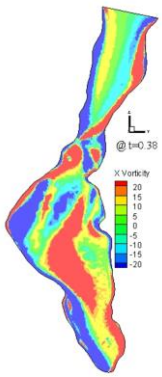
Patient A Coronal Plane	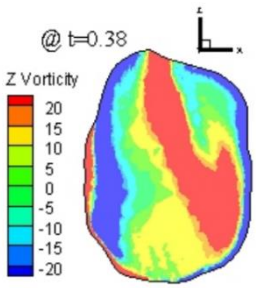
Patient B Sagittal Plane	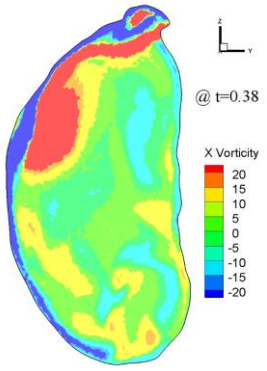

Fig. 5 Vorticity in the x-direction of the mid sagittal and vorticity in the z-direction of the mid coronal planes in AAA of patients A and B at peak systolic, decelerating and diastolic phases during the cardiac cycle

	a) t=0.25 (Peak Systole)
Patient A Pre	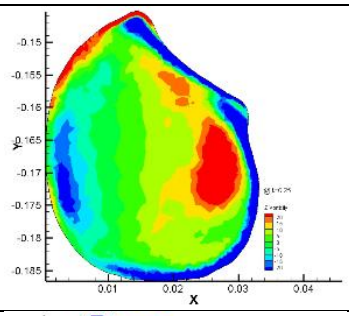
Patient A Post	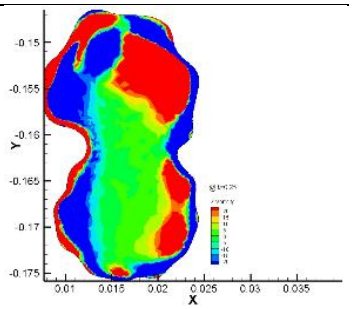
Patient B Pre	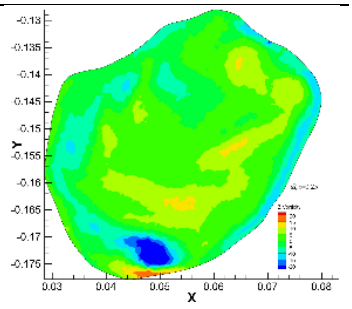
Patient B Post	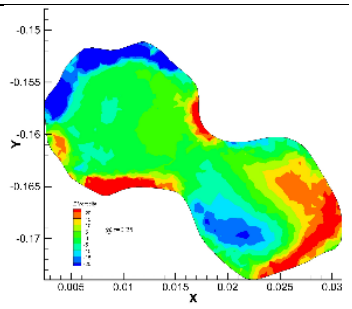
	b) t=0.38 (Mid Deceleration)
Patient A Pre	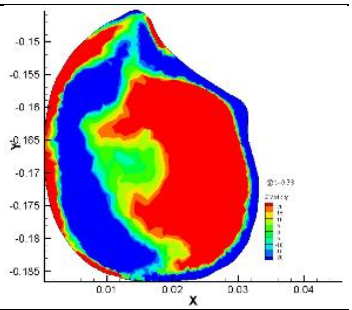
Patient B Coronal Plane	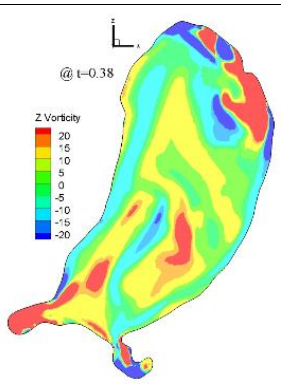
	c) t=0.5 (Early Diastole)
Patient A Sagittal Plane	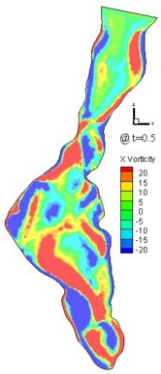
Patient A Coronal Plane	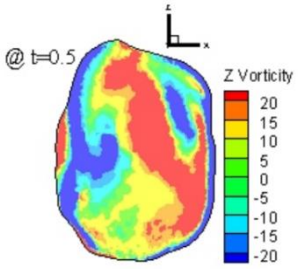
Patient B Sagittal Plane	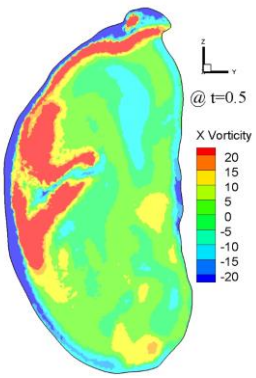
Patient B Coronal Plane	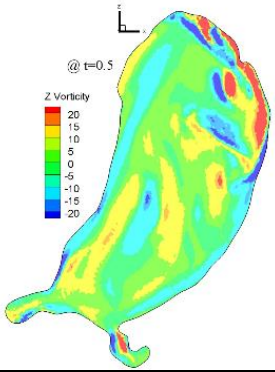

Patient A Post	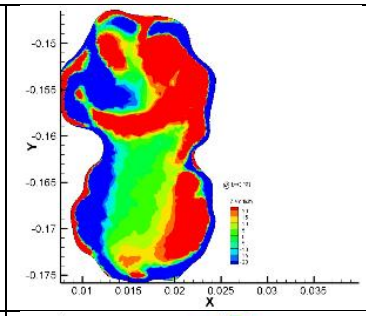
Patient B Pre	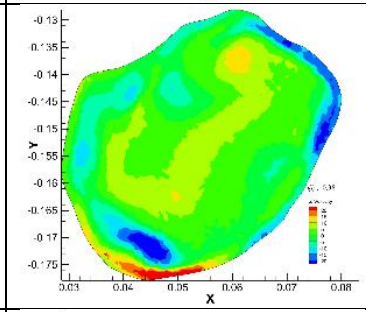
Patient B Post	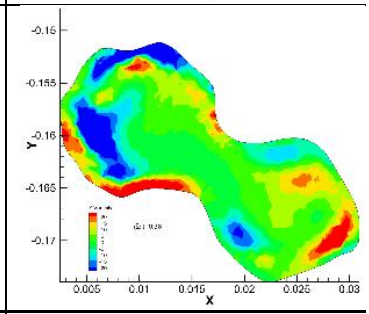
	c) t=0.5 (Early Diastole)
Patient A Pre	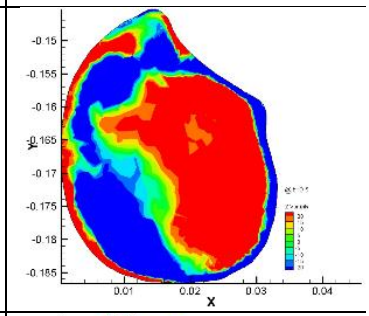
Patient A Post	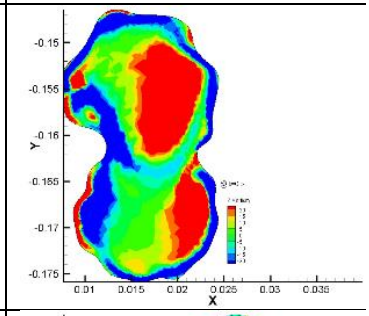
Patient B Pre	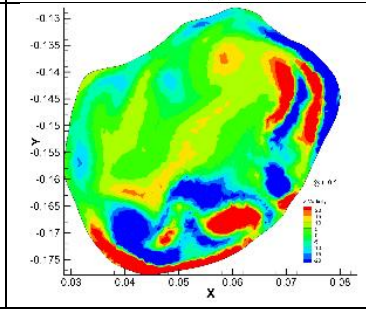

Patient B Post	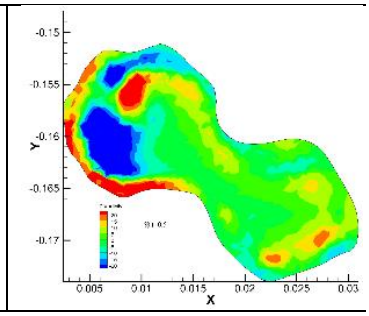

Fig. 6 Streamwise vorticity in the transverse mid plane in before and after procedures of patients A and B at peak systolic, decelerating and diastolic phases during the cardiac cycle

	a) t=0.25 (Peak Systole)
Patient A Pre	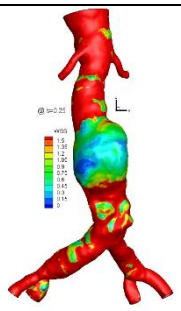
Patient A Post	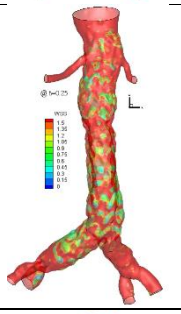
Patient B Pre	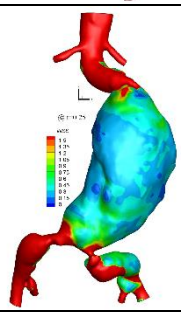

Patient B Post	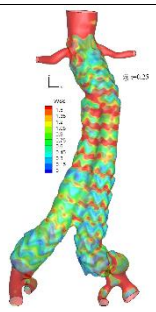
Healthy AA	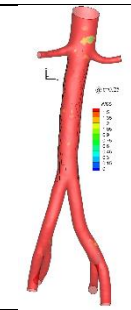
	b) t=0.38 (Mid Deceleration)
Patient A Pre	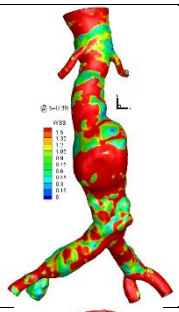
Patient A Post	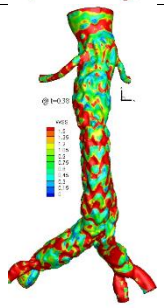
Patient B Pre	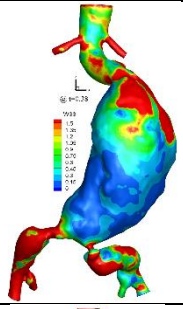
Patient B Post	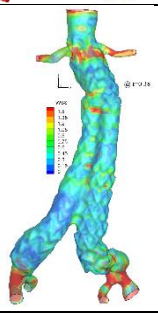

Healthy AA	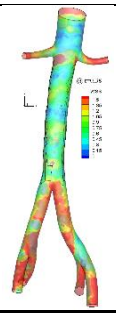
	c) t=0.5 (Early Diastole)
Patient A Pre	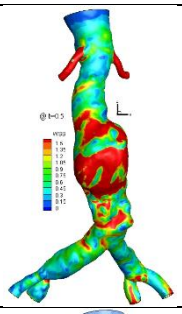
Patient A Post	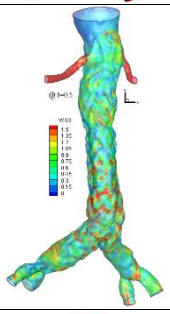
Patient B Pre	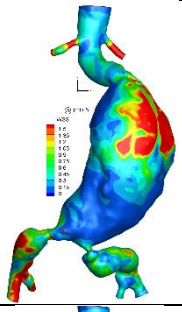
Patient B Post	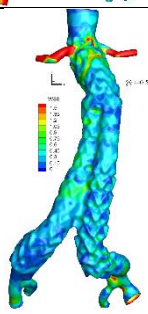
Healthy AA	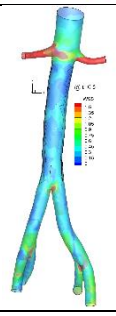

Fig. 7 Comparison of wall shear stress distributions in normal artery and that of AAA models of patients A and B at peak systolic, decelerating and diastolic phases during the cardiac cycle

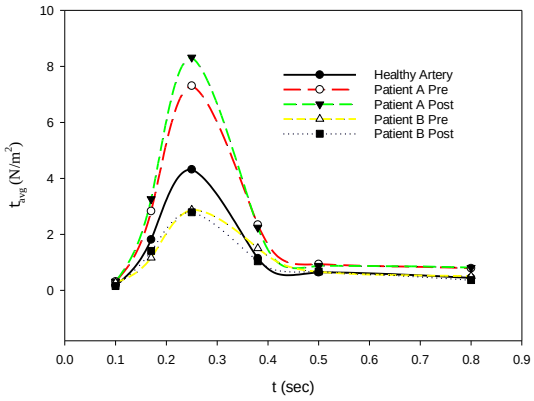

Fig. 8 Averaged magnitude of WSS along the surface of AAA for patient A and B